ADVANCED HEALTHCARE MATERIALS
www.advhealthmat.de

Engineering Lipid-Based Pop-up Conductive Interfaces with PEDOT:PSS and Light-Responsive Azopolymer Films

*Luca Terenzi, Ziyu Gao, Mehdi Ravandeh, Chiara Fedele, Lasse Hyldgaard Klausen, Claudia Latte Bovio, Arri Priimagi, and Francesca Santoro**

Significant challenges have emerged in the development of biomimetic electronic interfaces capable of dynamic interaction with living organisms and biological systems, including neurons, muscles, and sensory organs. Yet, there remains a need for interfaces that can function on demand, facilitating communication and biorecognition with living cells in bioelectronic systems. In this study, the design and engineering of a responsive and conductive material with cell-instructive properties, allowing for the modification of its topography through light irradiation, resulting in the formation of "pop-up structures", is presented. A deformable substrate, composed of a bilayer comprising a light-responsive, azobenzene-containing polymer, pDR1m, and a conductive polymer, PEDOT:PSS, is fabricated and characterized. Moreover, the successful formation of supported lipid bilayers (SLBs) and the maintenance of integrity while deforming the pDR1m/PEDOT:PSS films represent promising advancements for future applications in responsive bioelectronics and neuroelectronic interfaces.

1. Introduction

In the rapidly evolving field of bioelectronics, the development of advanced electronic materials for cell-instructive interfacing has emerged as a pivotal area of research. In particular, in organic bioelectronics, conducting polymers or organic semiconductors, stands out due to its unique properties such as flexibility, biocompatibility, and ease of processing.[1–3] These properties also contribute to the design of biomimetic electronic interfaces capable of interacting with living organisms and biological systems, such as neurons, muscles, and sensory organs.[3,4]

Furthermore, efforts have been made to enhance the interaction between cells and electronics by developing substrates with 3D structural features at the nano and microscale, transitioning from passive to active interfacing,[5,6] aiming for long-term integration and limited immune response to foreign devices.[5,7] Moreover, the design of these surface materials also favors the formation of an abiotic/biotic electronic interface to create a more biomimetic native tissue-like assembly,[8] where active adaptation remains a major feature yet to be achieved.[9]

In this scenario, materials capable of responding on demand to the surrounding environment and various stimuli are required. For example, light-driven materials containing photoresponsive compounds, such as azobenzene-containing polymers, can be employed for surface morphing, achieving biomimetic nano- and microstructures and engineering interfaces from 2D to 3D architectures by exploiting diverse light stimulation conditions.[10–12] In the presence of cells, it has been

L. Terenzi, Z. Gao, M. Ravandeh, F. Santoro
Institute of Biological Information Processing – Bioelectronics IBI-3
Forschungszentrum Jülich
52428 Jülich, Germany
E-mail: f.santoro@fz-juelich.de
L. Terenzi, Z. Gao, M. Ravandeh, F. Santoro
Neuroelectronic Interfaces
RWTH Aachen
52074 Aachen, Germany

C. Fedele, A. Priimagi
Faculty of Engineering and Natural Sciences
Tampere University
Tampere FI-33720, Finland
L. H. Klausen
Interdisciplinary Nanoscience Center – INANO-Fysik
Aarhus University
Aarhus 8000, Denmark
C. L. Bovio, F. Santoro
Center for Advanced Biomaterials for Healthcare
Italian Institute of Technology
Naples 80125, Italy
C. L. Bovio
Dipartimento di Chimica, Materiali e Produzione Industriale
University Federico II of Naples
Naples 80125, Italy

The ORCID identification number(s) for the author(s) of this article can be found under https://doi.org/10.1002/adhm.202303812

DOI: 10.1002/adhm.202303812

shown that precise control of the cell response can be achieved, including tuning the membrane curvature and cytoskeleton structure at the morphing material-cell interface.[13] Moreover, surface patterning can also be used within a cellular network to regulate cell growth and migration.[14]

These light-driven adaptive platforms have already found major applications in tissue engineering, electroactive biomaterials, and devices, primarily exploiting light for optoelectronic stimulation of cells, also through the use of organic semiconductors[15] and biohybrid interfaces.[16]

However, achieving adaptive bioelectronics with simultaneous maintained electric modulation and physical deformation at the microscale is still to be accomplished. Furthermore, adaptive electromechanical devices also require surface functionalization, and "fluid coatings" (e.g., the use of lipid bilayers) could better resemble the dynamicity of the native cell environment, as well as reconstitute protein assemblies and structures of the plasma membrane in vitro.

In fact, promising results have been achieved by exploiting supported lipid bilayers (SLBs) assembled onto conductive polymers to emulate plasma membrane fluidity and composition while simultaneously exploiting the mixed ionic-to-electronic conduction mechanism of the polymers for sensing.[17,18] By modulating the lipid composition, charge, and stiffness,[19] SLBs could resemble actual membrane and transmembrane assemblies for better integration with bioelectronic devices.[20,21] Recent research on SLB assembly on organic electronic platforms, such as PEDOT:PSS films and organic electrochemical transistors (OECTs), has demonstrated advantages in creating biomimetic electronics for sensing, monitoring protein activity, and potentially interfacing with cells.[22,23]

Particularly, recent progress in azopolymer-integrated lipids has achieved light-driven control over lipid bilayer structures and light-responsive membrane protein interactions,[24–27] toward recognizable cell-cell interactions and programable biohybrid systems.[28]

Here, we present an organic light-deformable conductive bilayer material integrating the poly(Disperse Red 1) methacrylate (pDR1m) azopolymer and PEDOT:PSS to obtain a responsive and light-controllable electromechanical bioelectronic platform. Various responsive patterning conditions have been investigated, including the formation of pop-up pillar-like structures emerging on demand from the 2D film. Moreover, the achieved platform can monitor the formation of SLBs and their active reshaping onto 3D pop-up structures upon light exposure.

The proposed platform provides a proof of concept for bioinstructive electronics, offering potential applications in brain-machine interfaces, tissue engineering, drug delivery, and biosensors.

2. Manufacturing and Morphological Characterization

Monolayers of pDR1m, PEDOT:PSS, and pDR1m/PEDOT:PSS bilayer films were achieved via spin coating on glass and ITO substrates (Experimental Section). Here, PEDOT:PSS was supplemented with either 0.02% or 1% dodecylbenzenesulfonic acid (DBSA) to investigate its influence on the material's mechanical properties (i.e., deformability) and conductivity. Furthermore, annealing and evaporation of remaining solvents of the conductive polymer were carried out either at room temperature (RT) or at 140 °C (**Figure 1a**).

The thickness of the resulting films was evaluated via profilometer and focused ion beam $^{-1}$scanning electron microscopy as 260 ± 10 nm for pDR1m, 95 ± 7 nm, and 87 ± 6 nm for PEDOT:PSS with 0.02% and 1% DBSA, respectively. The Young's modulus of pDR1m/PEDOT:PSS films was also evaluated through quantitative nanomechanical analysis with atomic force microscopy (AFM), leading to values in the order of GPa, which suggest possibly a predominant effect of the rigid support underneath the spin-coated films (Table S1, Supporting Information).

For the formation of the SLBs at the PEDOT:PSS film surface, roughness and wettability have been considered because of their key role in favoring micelle rupture to form a homogeneous and fluid lipid bilayer. Here, the surface roughness of the films was characterized via AFM: Figure 1b–d shows a higher average surface roughness with both the increase of the DBSA concentration in the PEDOT:PSS solution and the annealing temperature of the films (Ra = 1.3 ± 0.05 nm at RT, Ra = 3.5 ± 0.15 nm at 140 °C, 1% DBSA, where Ra refers to the average of the individual heights and depths from the arithmetic mean elevation of the surface),[27] whereas for mono- and bilayers at both annealing temperatures, 0.02% DBSA samples presented comparable surface roughness.

Then, contact angle measurements (Figure 1e) indicated a more hydrophilic surface when reducing the annealing temperature from 140 °C to RT, possibly due to low annealing temperatures retaining higher water absorption and hydrophilicity of the PEDOT:PSS polymer chain.[29,30] Moreover, increasing the DBSA concentration in both mono and bilayers from 0.02% to 1%, the contact angles of the bilayer structures decreased from 38.6 ° to 31.6 ° (RT-annealed sample) and from 72.1 ° to 63.5 ° (140 °C annealing temperature), respectively.

3. Electrochemical Characterization of Bilayer Films

To study the electrochemical properties of the pDR1m/PEDOT:PSS films on ITO-coated glasses, cyclic voltammetry (CV), and electrochemical impedance spectroscopy (EIS) measurements were carried out.

Here, oxidation peak currents ranging from −0.25 to 0.61 V and reduction peaks ranging from −0.31 to −0.48 V were observed in the I-V curves for the pDR1m/PEDOT:PSS bilayers, both with 0.02% and 1% DBSA (Figure 1f,g), while these peaks were not detected in the case of monolayer PEDOT:PSS films.

Redox peaks with higher current amplitudes were observed in the case of pDR1m/PEDOT:PSS films containing 1% DBSA (compared to the 0.02% case). Moreover, redox current amplitudes increased noticeably after annealing at 140 °C, for both 0.02% and 1% DBSA concentrations. These results suggest DBSA-content and annealing temperature-dependent electrochemical responses of the pDR1m/PEDOT:PSS film structures, considering that the annealing temperature of 140 °C is higher than the glass transition temperature of pDR1m. This could possibly induce surface chemical interactions between PEDOT:PSS

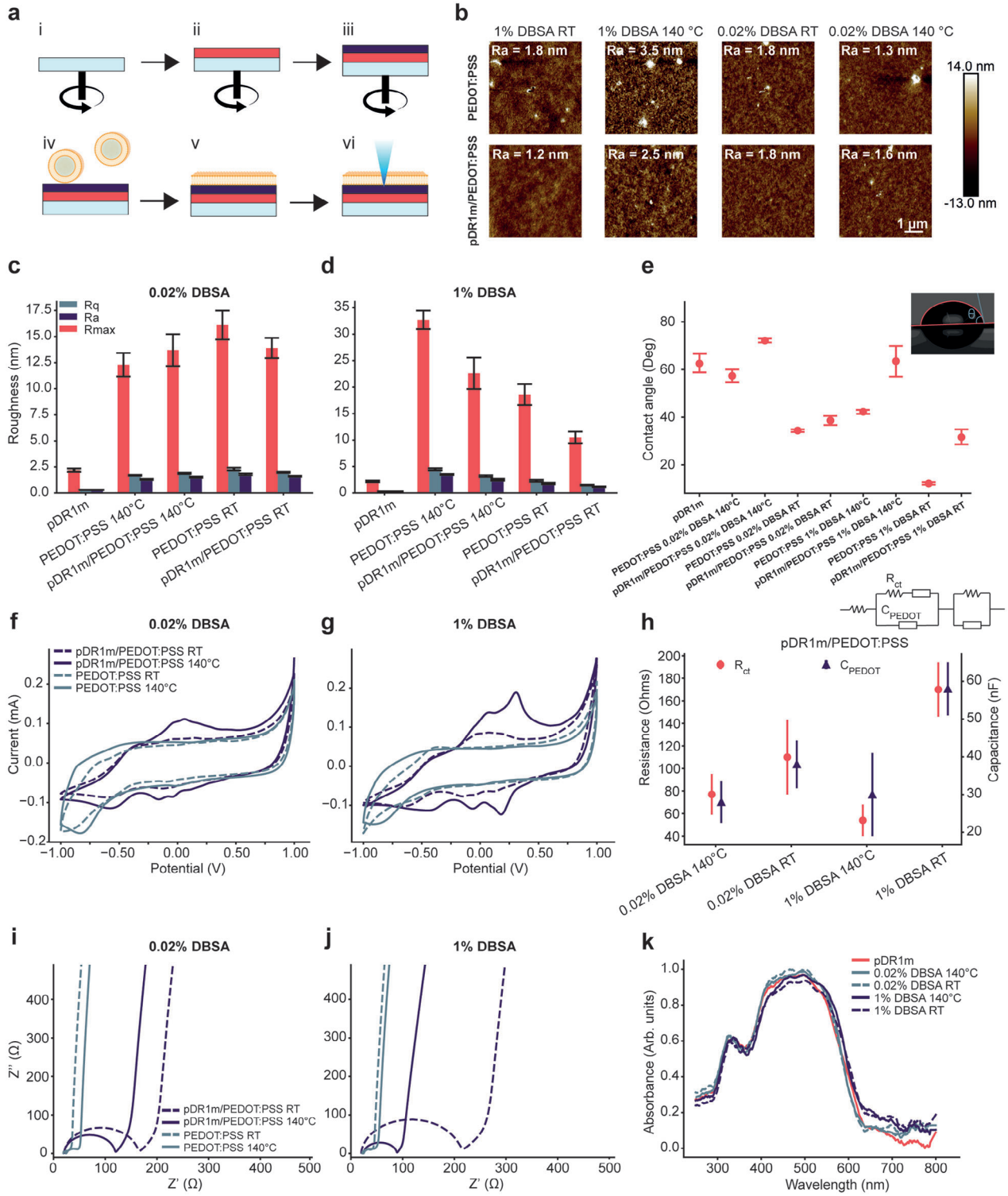

Figure 1. Manufacturing and characterization of the mono and multilayered samples: a) Manufacturing schematics of the starting glass substrate (i) on top of which the pDR1m (ii) and successively the PEDOT:PSS (iii) are spin-coated. The SLB is then formed on top of the pDR1m/PEDOT:PSS sample (iv – v), and FRAP experiments can be conducted (vi). b) AFM images for each sample used for roughness characterization. The roughness results (mean ± SD) are reported in c,d) for 0.02% DBSA and 1% DBSA cases, respectively. e) Contact angle measurements results (mean ± SD) for the various samples. f,g) report the CV curves for 0.02% DBSA and 1% DBSA samples, respectively. h) Values (mean ± SD) of charge transfer resistance (R_ct) and capacitance (C_PEDOT) for the pDR1m/PEDOT:PSS samples. The fitting circuit used and the corresponding elements are also shown. i,j) show a zoom-in at high frequencies for EIS curves for 0.02% and 1% DBSA samples, respectively. k) Absorption spectra for pDR1m and pDR1m/PEDOT:PSS samples.

and pDR1m polymer chains, leading to higher redox peak currents.

In addition, EIS measurements of monolayers indicated a typical dielectric behavior of pDR1m films (predominant capacitive component, Figures S1,S2 and Table S2, Supporting Information), where resulting Nyquist plots were fitted with an R-(R, CPE) circuit. Impedance spectra of PEDOT:PSS monolayers with different DBSA concentrations and annealing temperatures were fitted with a Randall circuit including a Warburg element, to model the kinetic diffusion of charges only for a finite length in proximity to the PEDOT:PSS surface.[31]

The results shown in Figure 1h present lower charge transfer resistances (Rct) for the PEDOT:PSS layers in the cases of higher DBSA concentration (1%) and higher annealing temperature (140 °C; Table S2, Supporting Information). This is also in agreement with previous reports showing that increasing DBSA concentration and annealing temperature in PEDOT:PSS films would decrease the resistivity of the conductive polymer film.[32–35]

Subsequently, impedance spectra of pDR1m/PEDOT:PSS bilayer films were instead fitted considering an electrical equiv. circuit resulting from the series of the two circuits discussed earlier for monolayer films (Figure 1f). Here, pDR1m/PEDOT:PSS films presented a slightly higher Rct than PEDOT:PSS monolayers, as shown in Figure 1i,j, where the Nyquist plots (0.02% and 1% DBSA respectively) depict the Rct increase with the increasing diameter of the half circumference of the impedance spectrum curves. The lowest Rct was exhibited in the pDR1m/PEDOT:PSS samples with 1% DBSA and 140 °C annealing temperature.

Finally, the electrochemical stability of both PEDOT:PSS and pDR1m/PEDOT:PSS films with 1% DBSA was investigated through EIS in aqueous Dulbecco's phosphate buffer solution (DPBS; Figure S3, Supporting Information), showing no delamination or visible degradation after 24 h. The major difference observed was an increase in the charge transfer resistance in all conductive films, mainly due to swelling effects of PEDOT:PSS.[36]

4. Light-Driven Deformation of the pDR1m/PEDOT:PSS Bilayers

To understand the light-response of pDR1m/PEDOT:PSS films and the maximum stimulation wavelength, UV-Vis absorption spectra were measured. Due to the wavelength-dependent photo-switching capability of pDR1m, it was of interest to characterize the absorption spectra of both bare pDR1m and pDR1m/PEDOT:PSS samples to ensure that the PEDOT:PSS layer would not alter the optical properties of the material. As shown in Figure 1k, pDR1m/PEDOT:PSS films presented an absolute maximum peak ≈480 nm, similar to the bare pDR1m sample. The results confirmed that the PEDOT:PSS layer has no influence on the light absorption property of the pDR1m polymer, regardless of DBSA concentration and annealing temperature.

In light of this, for further experiments, only pDR1m/PEDOT:PSS samples annealed at 140 °C were considered, given their higher conductivity as well as surface roughness and wettability, which are relevant features for the formation and monitoring of the SLBs. These samples exhibited better conductivity than those kept at RT. Hence, light-driven patterning was conducted for the samples annealed at 140 °C.

For surface patterning, two different laser setups were employed: the Lloyd's mirror interferometer (Figure S4, Supporting Information) and laser scanning confocal microscope (**Figure 2**, with monodirectional or bidirectional scanning modes). The 488 nm laser was chosen to maximize the light-driven response of pDR1m/PEDOT:PSS bilayers based on the UV-Vis absorption spectra.

For the Lloyd's mirror patterning, the microtopography period Λ was set to 1.5 and 2.5 µm, determined by $\Lambda = \lambda/2\sin\theta$, where λ is the wavelength of the laser (488 nm) and θ is the angle between the mirror and the laser beam. As shown in Figure S4a–c (Supporting Information) for the pDR1m monolayer, the pattern modulation depth appears higher for the 2.5 µm period, but the crests of the patterns appear more irregular. Here, the resulting patterning area is large (0.25 cm^2) with surface modulations in the order of 100–200 nm. On the other hand, the modulation in the pDR1m/PEDOT:PSS patterned samples appeared significantly lower than in the pDR1m ones (Figures S5 and S6, Supporting Information). This is also evidenced by the diffraction efficiency (DE) analysis in Figure S4b,c (Supporting Information). The DE for pDR1m/PEDOT:PSS samples was much smaller compared to that for pDR1m, indicating negligible SRGs were formed, as also shown in AFM measurements.

In addition, a laser scanning confocal microscope was used to create the patterns by exposing 488 nm laser light through a horizontal ROI (0.48 × 24 μm^2), either bidirectionally (i.e., the laser spot scans the ROI left to right, then right to left, and then repeats) or monodirectionally (i.e., the laser spot scans the ROI left to right, turns off, goes back to the left, and then repeats), as illustrated in Figure S4d (Supporting Information).

In bidirectional scanning mode, different conditions were investigated for pDR1m films, including focal plane position (±7 µm vertical displacement to the surface plane of the polymer film, as shown in Figure S7, Supporting Information), laser power (ranging from 2.5% to 40%), and exposure time (15–90 s).

Light-patterning experiments with different exposure times were carried out on pDR1m samples with the fixed laser power set to a nominal 5% and bidirectional scanning mode (Figure 2bi). However, the effective laser intensity at the sample plane could not be estimated. It was observed that after 30–45 s, the height of the pattern would reach a saturation point (541 ± 29 nm), similar to its width (2.51 ± 0.08 µm), as shown in Figure 2bii-iii. Therefore, the exposure time for pDR1m and pDR1m/PEDOT:PSS films was set to 30 s for further light-driven quantification.

Different laser powers were tested to optimize the stimulating intensity for pDR1m/PEDOT:PSS films: a series of laser powers, starting from 5% with a 5% increase at each step, were carried out. A minimum of 15% laser power was required to achieve visible light-driven patterns, as shown in Figure 2c,d. Furthermore, the 30% intensity was confirmed as the maximum intensity to limit any possible mechanically induced damage to the PEDOT:PSS layer (Figure S8, Supporting Information).

Moreover, for laser powers higher than 15%, light-inscribed patterns appeared more irregular in pDR1m/PEDOT:PSS (Figure 2ci,di). A consistent lateral accumulation on the left side of the ROI was observed in pDR1m/PEDOT:PSS patterns, possibly due to the photofluidization of the pDR1m polymer.[37]

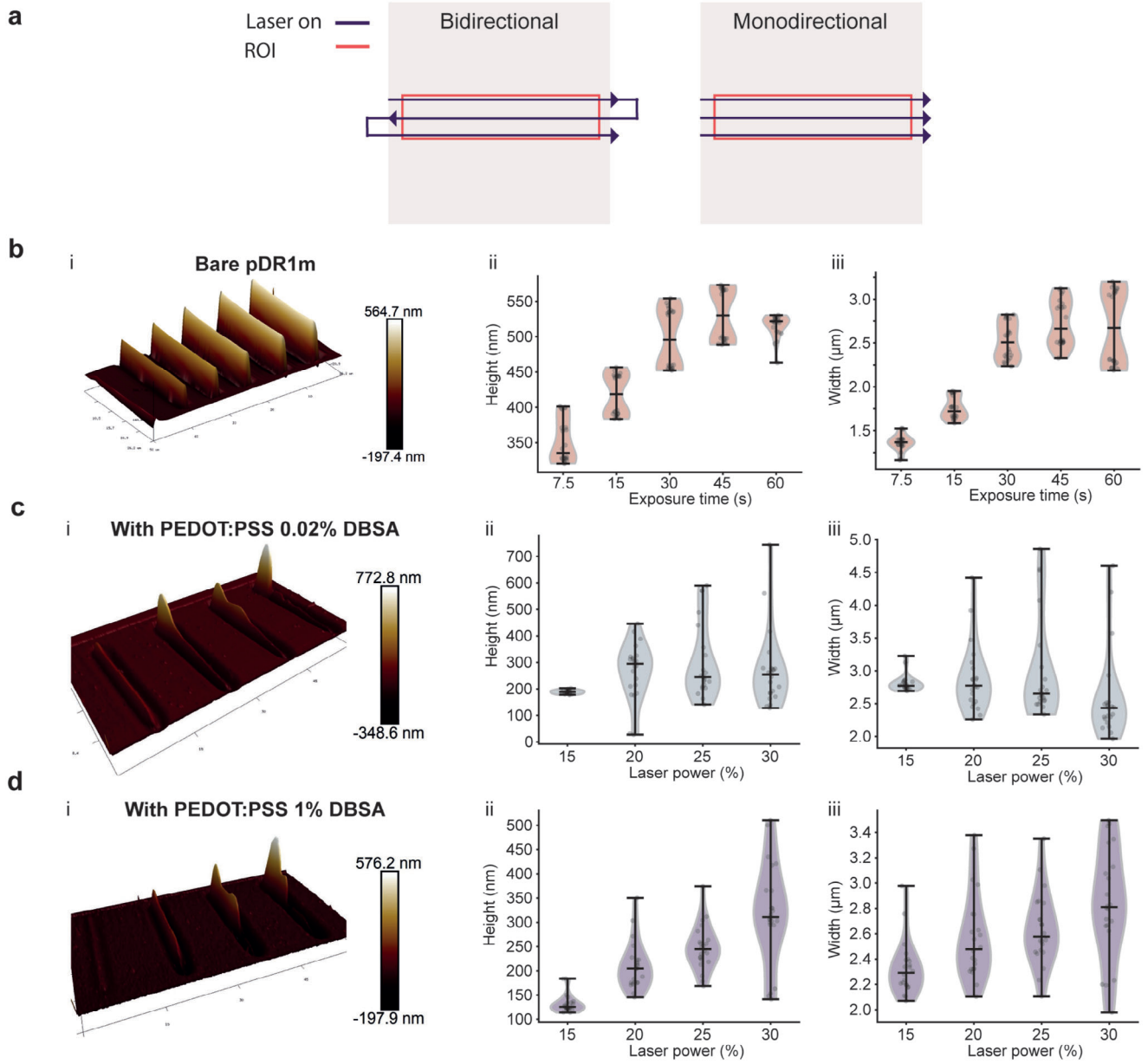

Figure 2. Laser confocal microscope bidirectional patterning. a) Illustration of the two confocal microscope scanning modalities. b) AFM image (i) of pDR1m sample patterned with confocal microscope in bidirectional scanning mode at different exposure times. The heights (ii) and widths (iii) of the two analyzed replicates are also reported. c) AFM image (i) of pDR1m/PEDOT:PSS samples annealed at 140 °C with 0.02% DBSA patterned with confocal microscope in bidirectional scanning mode at different laser powers. The heights (ii) and widths (iii) of the two analyzed replicates are also reported. d) Same imaging and patterning conditions as in c) but for 1% DBSA containing pDR1m/PEDOT:PSS samples annealed at 140 °C.

The hypothesis for this behavior is that the laser scanning motion and high laser power lead to an unbalanced force exerted on the azopolymer, pushing it to accumulate on one side of the ROI. An increase in the laser power determines higher patterns but also accentuates the lateral accumulation and irregularities.

When patterning with the confocal microscope under monodirectional scanning mode, the lateral accumulation was further enhanced by the asymmetric motion of the laser spot.

In the light-patterning experiments of pDR1m films at different laser powers and in monodirectional scanning mode, the resulting pillar-like structures achieved heights of up to 3 µm after 30 s stimulation with 20% laser power, as shown in **Figure** 3a. However, both lower (15%) and higher (25% and 30%) laser powers resulted in smaller light-driven pillar height values. Here, possibly unconstrained pDR1m surface topography could undergo inverse mass displacement, reducing the final height of the pattern.[38]

In Figure 3aiii, a marked bimodal data distribution for the pattern's aspect ratio is noticeable, which decreases with the increase in laser power. This is primarily due to the differences between

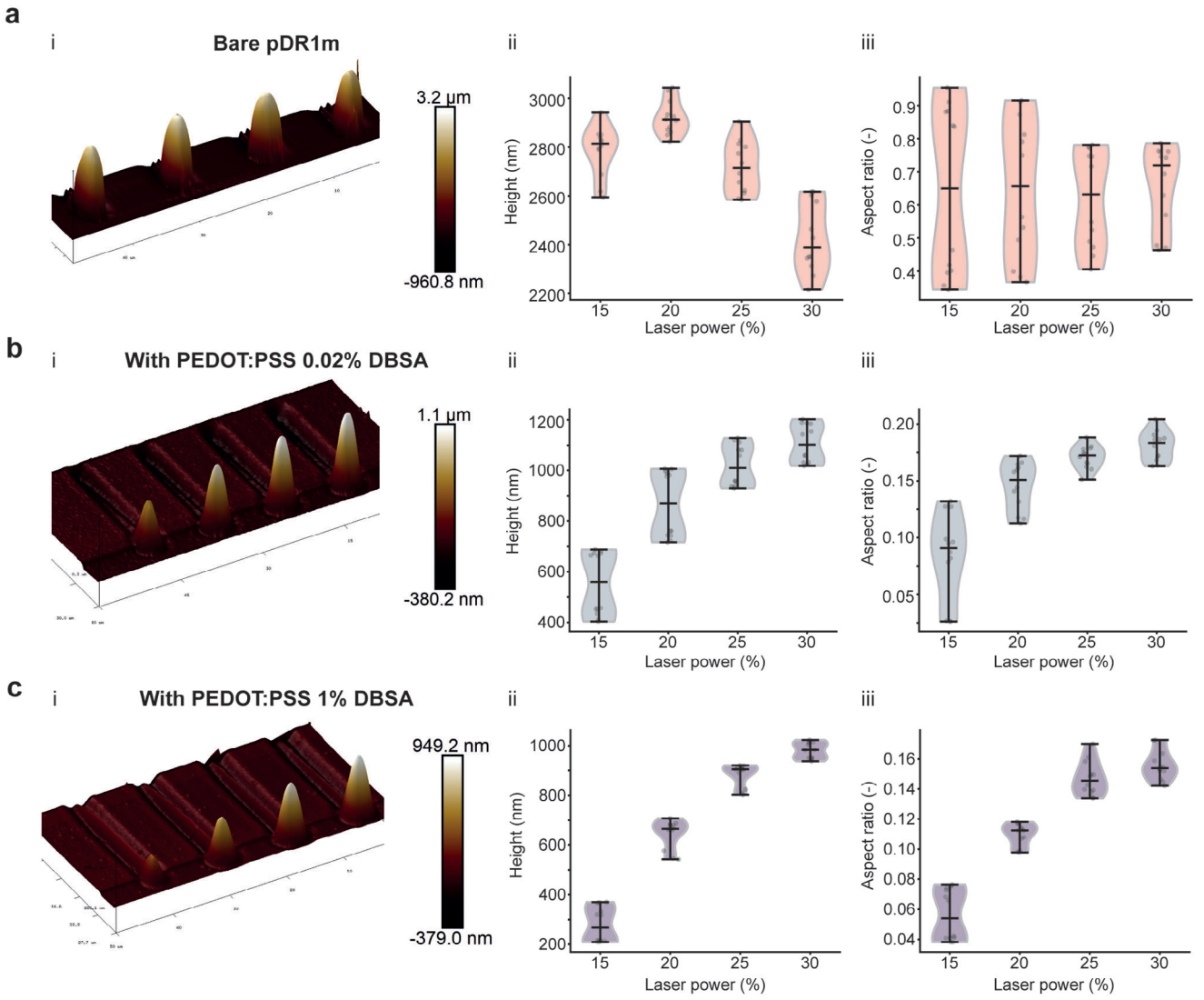

Figure 3. Confocal microscope monodirectional scanning patterning and lateral accumulation. a) AFM image (i) of pDR1m samples patterned with confocal microscope in monodirectional scanning mode at different laser powers. The heights (ii) and aspect ratio (iii) of the two analyzed replicates are also reported. b,c) Same imaging and patterning conditions as in a) but for pDR1m/PEDOT:PSS samples annealed at 140 °C with 0.02% and 1% DBSA respectively.

longitudinal and transversal widths (compared to the ROI orientation).wer the laser power, the less polymer accumulation occurs on the left side of the ROI, leading to a longitudinal width larger than the transversal one.

In the case of pDR1m/PEDOT:PSS, monodirectional scanning accentuates the lateral accumulation for both the 0.02% and 1% DBSA samples, as presented in Figure 3b,c. Here, the patterns' height increased to over 1 µm following the laser power increase from 15 to 30%. A similar trend was also observed in the aspect ratio with decreased variation, suggesting that the resulting pillar-like structure has increased circular symmetry. It is hypothesized that the top layer of the PEDOT:PSS polymer could generate a rotationally symmetric force on the photofluidized pDR1m during lateral accumulation, leading to more symmetric pillar-like structures.

Furthermore, the interface coupling and deformation between the pDR1m and PEDOT:PSS polymers were investigated with focused ion beam – scanning electron microscopy (FIB-SEM). As indicated in Figure S9 (Supporting Information), the interface between the pDR1m and PEDOT:PSS layers in the pDR1m/PEDOT:PSS 1% DBSA 140 °C sample appeared well-defined with smooth adhesion in the static case, and no visible damage to the PEDOT:PSS layer was observed after light-driven deformation.

Overall, the pDR1m/PEDOT:PSS samples appeared stable under light-patterning with 488 nm laser, giving controllable deformation from planar film structure to pillar-like structure with up to 1.2 µm height. This allowed to create active morphing electrodes from 2D to 3D with PEDOT:PSS polymer substrates.

5. SLB Assembly

Two annealed pDR1m/PEDOT:PSS substrates at RT and 140 °C containing 1% DBSA were used for the assembly of SLBs through the vesicle fusion method. Unlike the PEDOT:PSS film, the presence of hydrophobic pDR1m makes this pDR1m/PEDOT:PSS substrate a challenging platform for vesicle fusion, since SLB formation occurs preferentially on very smooth and hydrophilic surfaces through this method.[39] Various methods can induce vesicle fusion under non-ideal conditions, including temperature, pH, osmotic pressure, and shear stress.[22,40–42] In this work, osmotic pressure was used to induce vesicle fusion on pDR1m/PEDOT:PSS substrates by slowly adding deionized (DI) water to a liposome solution incubated with the substrate. The successful formation of SLBs was studied using CV, EIS, and fluorescence recovery after photobleaching (FRAP) techniques.

CV measurements confirmed the formation of lipid bilayers on both substrates, as evidenced by the disappearance of characteristic peaks in the pDR1m/PEDOT:PSS voltammogram (oxidation between 0 and 0.17 V and reduction between −0.18 and 0.1 V). This disappearance indicated that the lipid bilayer hindered electron transfer between the electrolyte and the polymer film (see **Figure** 4a).[43,44]

To gain further insights into the lipid bilayer structure, the electrical sealing properties of the bilayer formed on both substrates were monitored by EIS. Figure 4b (Bode plot) illustrates significant impedance changes before and after SLB formation, particularly in the mid-frequency range of 10–10 000 Hz, typically attributed to lipid bilayers.[22,41,42,45] Notably, the pDR1m/PEDOT:PSS substrate treated at room temperature exhibited higher impedance compared to the substrate annealed at 140 °C. Upon bilayer formation, the pDR1m/PEDOT:PSS Bode plot exhibited an increase in impedance magnitude at the mid-frequency range, indicating the formation of an additional resistive layer on top of the PEDOT:PSS. In contrast, the annealed substrate at 140 °C showed a smaller change in impedance. These results are consistent with AFM roughness measurements (Figure 1b) and wettability (Figure 1e) results for the two substrates; the room temperature substrate showed lower surface roughness and higher wettability compared to the substrate annealed at 140 °C. The lower impedance of the 140 °C substrate may be attributed to the partial formation of a lipid bilayer on this substrate due to its greater hydrophobic nature.

Additionally, impedance phase values (Figure S10, Supporting Information) revealed a transition shoulder region with a lower phase angle, indicative of a new resistive component arising from the presence of the bilayer. A lipid bilayer should be impermeable to ion flow, leading to increased resistance. However, the presence of pores in the lipid bilayer or partial bilayer formation on substrates can decrease impedance, allowing ions to pass through the pores and reach the electrode's surface.[22] Furthermore, Figure S11 and Table S4 (Supporting Information) present EIS results based on Nyquist plots for different electrodes. To fit the data, a similar equiv. circuit for pDR1m/PEDOT:PSS (Figure S2c, Supporting Information) was used to characterize the electrical properties of the SLB. Based on fitted results from the Nyquist plot, the SLB formation can be confirmed with an increase in Rct.

In addition to EIS, to confirm vesicle fusion on pDR1m/PEDOT:PSS films, we utilized the FRAP technique, a commonly employed optical method for determining surface fluidity (lateral diffusion within the 2D plane of SLBs).[22] After irreversibly photobleaching fluorophore-labeled lipids in a defined region, the recovery of fluorescence intensity was monitored for 7 min. The diffusion coefficient (D) was calculated based on the equation, $D = \omega^2/4\tau_{1/2}$, where ω is the radius of the photobleached spot and $\tau_{1/2}$ is the time needed to reach half of the maximum recovery intensity. FRAP experiments were conducted on both substrates (Figure 4c,f) and were used to confirm SLB formation and monitor real-time morphological changes in the pDR1m/PEDOT:PSS substrate during FRAP experiments with a 561 nm laser, as the 488 nm laser could alter the morphology of pDR1m/PEDOT:PSS.

While some recovery of the photobleached spot was observed in all samples (Figure 4d–h), there was a clear difference in diffusion coefficients for SLBs on substrates. The diffusion coefficient for pDR1m/PEDOT:PSS annealed at room temperature and 140 °C was 1.64 $\mu m^2 s^{-1} \pm 0.38\ \mu m^2 s^{-1}$ and 0.1 $\mu m^2 s^{-1} \pm 0.01\ \mu m^2 s^{-1}$, respectively. Figure 4c,f illustrates the changes in the fluorescence recovery of SLB and the morphological changes of both substrates after bleaching with a 561 nm laser. Notably, the recovery occurred over half of the region of interest (ROI) in room temperature substrates (Figure 4c), while there was almost no recovery after photobleaching in the SLB on annealed substrates at 140 °C (Figure 4f). The smaller diffusion coefficient for substrates at 140 °C may be attributed to the substrate's hydrophobic nature, which enhances the interaction of the electrode with alkyl chains in the lipid bilayer, thus restricting the lateral mobility and diffusion of lipid molecules within the bilayer.

6. Conclusion

In this work, a light-driven conductive deformable substrate was achieved by coupling the light-sensitive pDR1m azopolymer with the organic conductive polymer PEDOT:PSS. Here, resulting roughness, wettability, electrochemistry, light response, morphology, and its potential to engineer lipid bilayers were discussed. The critical role of DBSA concentration and annealing temperature was shown to regulate the surface roughness and hydrophilicity of the PEDOT:PSS layer. From the electrochemical characterization, CV voltammograms showed higher oxidation and reduction currents in the 1% DBSA samples and 140 °C annealed samples, while EIS measurements highlighted a low charge transfer resistance in films containing 1% DBSA. In the light-driven study, periodic surface patterns were achieved both with Lloyd mirror and confocal patterning. However, high aspect ratio and pop-up pillar-like structures were only achieved in the case of monodirectional confocal laser exposure. Finally, SLBs were successfully formed and maintained in their integrity and diffusivity while creating an emerging pillar structure in the pDR1m/PEDOT:PSS film. In turn, the presented platforms provided concepts for further integration into micro-nano electronic devices and cell interfacing with lipid surface functionalization, allowing addressable active control of emerging pop-up organic and conductive electrode interfaces. Scaling down the electronic evaluation resulting from the light-driven deformation is suggested for future applications as electrodes.

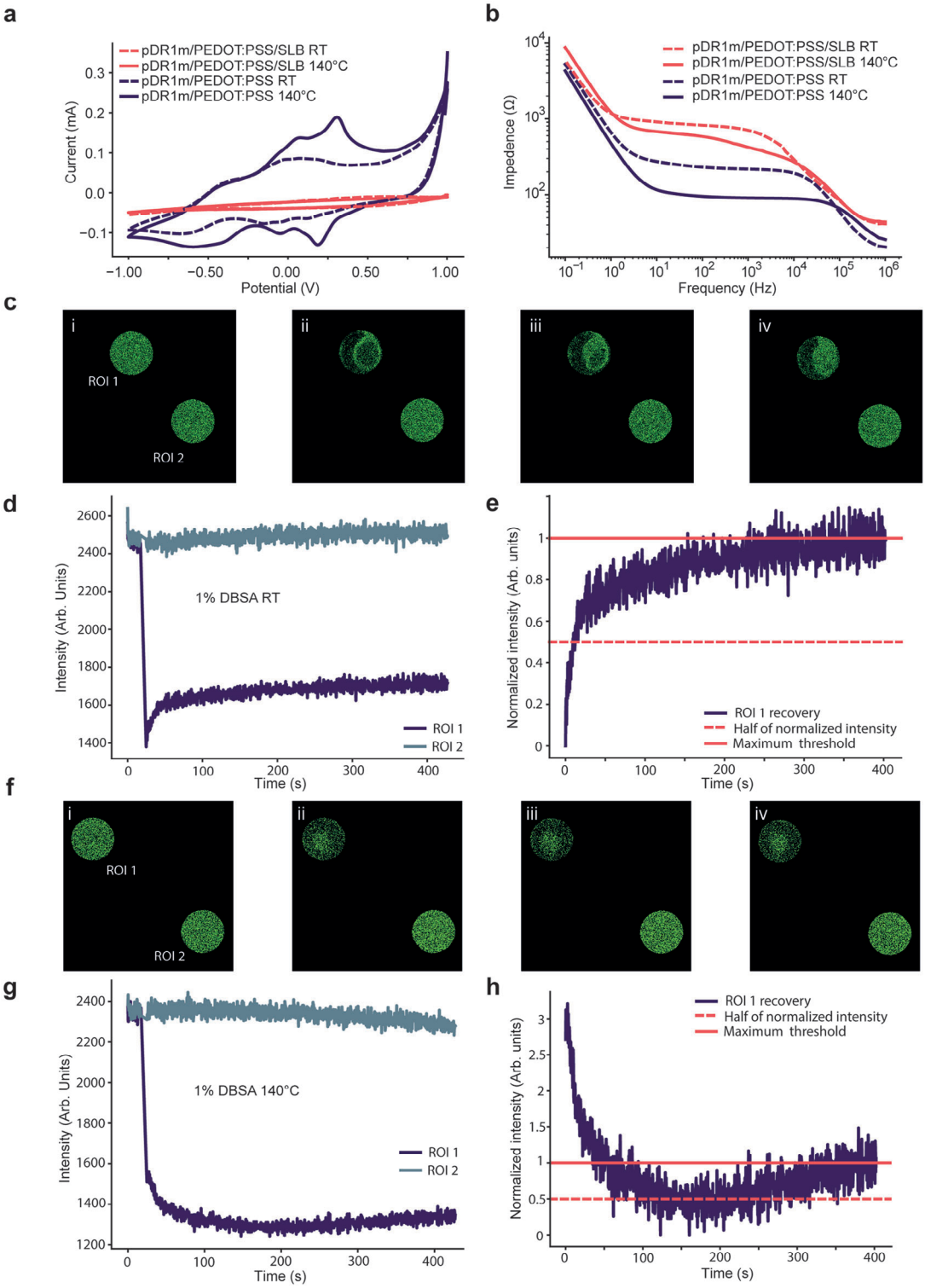

Figure 4. Characterization of POPC lipid bilayer formation on different substrates: a) Cyclic voltammograms of pDR1m/PEDOT:PSS (annealed at RT and 140 °C) before and after formation of lipid bilayer in DPBS buffer (scan rate 50 mV/s) b) Electrochemical impedance analysis (Bode plot) PDR1m/PEDOT:PSS (annealed at RT and 140 °C) before and after formation of lipid bilayer in DPBS buffer c,f) FRAP micrographs showing the recovery of Texas Red SLBs on pDR1m/PEDOT:PSS RT and pDR1m/PEDOT:PSS 140 °C, respectively at pre-bleaching, bleaching, post-bleaching and recovery (from left to right) ROI 1 (bleached) and ROI 2 (control) areas d) The fluorescence intensity for ROI 1 (bleached) and ROI 2 (control) of Texas Red SLB on pDR1m/PEDOT:PSS RT e) The recovery fluorescence intensity values were normalized to the intensity of control of Texas Red SLB on pDR1m/PEDOT:PSS RT g) The fluorescence intensity for ROI 1 (bleached) and ROI 2 (control) of Texas Red SLB on pDR1m/PEDOT:PSS 140 °C h) The recovery fluorescence intensity values were normalized to the intensity of control of Texas Red SLB on pDR1m/PEDOT:PSS 140 °C.

7. Experimental Section

Sample Preparation: A bilayer of Poly(Disperse Red 1 methacrylate) (pDR1m, Sigma-Aldrich) and Poly(3,4-ethylenedioxythiophene):polystyrene sulfonate (PEDOT:PSS), together with pDR1m and PEDOT:PSS monolayers, were manufactured on either bare 15 mm diameter circular glass coverslips (Glaswarenfabrik Karl Hecht), or 30 mm diameter ITO coated ones (sputtered in ZMNT with Berlin Nordiko, NS2550 sputtering machine) by spin coating (Laurell Technologies Corporation). The cover slips were cleaned by ultrasound bath in subsequent sonication steps: 10 min in milliQ water, 10 min in acetone (99.5%, Chemsolute), and 10 min in isopropanol (99.8%, Chemsolute). The substrates were then dried under a nitrogen stream.

Solution of pDR1m with concentration of 5% (w/v) in chloroform (Sigma Aldrich) was prepared, sonicated for 30 min in ultrasound bath, and filtered with a 0.45 µm pores size PTFE filter (Macherey-Nagel). The filtered solution (15 µL for the small substrate and 40 µL for the big one) was dispensed on the glass cover slips spinning at 1500 rpm for 60 s.

PEDOT:PSS was prepared by mixing PH1000 (Heraeus), ethylene glycol 5% v/v (Sigma Aldrich), (3-Glycidyloxypropyl)Trimethoxysilane (GOPS, Sigma Aldrich) 1% v/v, and either dodecylbenzenesulfonic acid (DBSA, Sigma Aldrich) 0.02% or 1% v/v. The solution was then sonicated for 20 min and filtered with a 0.4 µm pores size filter (EMD Millipore). The solution (80 µL for the small substrate and 200 µL for the big one) was then statically spin coated at 2000 rpm for 120 s with an acceleration of 400 rpm.

Morphological Characterization: The thickness of the pDR1m and PEDOT:PSS layers was measured with a DekTak XT profilometer (Bruker) and a Focused Ion Beam – Scanning Electron Microscopy (FIB-SEM Helios NanoLab 600i and 650, Thermo Fischer). For the profilometer analysis, the drag speed used for the tip was 100 µm/s, with a contact force of 3 mN/cm. For the FIB-SEM imaging, the sample was coated with a 5 nm gold layer and milled with gallium ion beam (current: 0.79 nA; tension: 30 kV for milling and current: 0.23 nA; tension: 30 kV for polishing). Scanning electron micrographs were acquired in backscattered mode with the electron beam to 3 kV and 0.17 nA current.

The roughness analysis was carried out with AFM (Dimension Edge, Bruker) imaging using PeakForce tapping.

Samples Young's modulus was measured using PeakForce Quantitative Nanomechanical Mapping with RTESPA-525 probes (Bruker AFM Probes; nominal tip radius 8 nm, nominal spring constant 200 N/m, nominal resonance frequency 525 kHz). The absolute method was used to quantify tip radius with a rough Ti surface. The same probe was employed for the analysis of all samples and the tip radius measured before and after all experiments showing no change. Images were recorded at 128 × 128 pixels with a scan rate of 1 Hz and peak force of 500 nN.

For wettability characterization, a contact angle measurement system (OCA 20, Dataphysics) was used to dispense consistently the same volume of Milli-Q water (10 µL) on top of the surface of interest.

To measure the absorption spectra of the polymer's mono and bilayers, a UV-VIS spectrophotometer was used (Lambda 900 UV/VIS/NIR, PerkinElmer).

Electrochemical Characterization: For CV measurements, a three-electrode set up consisting of a working electrode (WE), a reference electrode (RE), and a counter electrode (CE) was used, together with a potentiostat (VSP 300, Biologic). The WE was contacted to the ITO coated substrate, while the RE (Ag/AgCl) and the CE (platinum wire) were immersed in the Dulbecco's phosphate buffer solution (DPBS, Thermo Fischer) inside a well glued on top of the spin coated polymer (bi)layer to investigate. The sinusoidal input signal was set to 50 mV amplitude and it swept a range of frequencies from 1 Hz to 100 kHz, averaging two measures per frequency.

Impedance spectra obtained from the samples were fitted with specific equiv. circuits mimicking the characteristics of the sample. The fitting was executed in python with a self-made script (Supporting Information) making use of impedence.py.

CV measurements were carried out following the same three electrodes set up as for the EIS ones. The potential range applied was between −1.0–1.0 V with a 100 mV/s scan speed, and the recorded current was obtained averaging over 10 voltage steps. For each CV acquisition a total of 3 cycles were measured, referring always to the second one to show the results.

Patterns Inscription and Imaging: To inscribe the SRGs both a confocal laser scanning microscope (LSM 880, Zeiss) and a Lloyd's mirror interferometer have been used, both in dry conditions.

In Lloyd's mirror interferometer, a 488 nm continuous-wave laser (Coherent Genesis CX488-2000) with circular polarization and an intensity of ≈500 mW/cm^2 over an area of 0.25 cm^2 for 20 min. The microtopography period Λ was set to 1.5 and 2.5 µm, and it was determined by $\Lambda = \lambda/2\sin\theta$, where λ is the wavelength of the laser and θ is the angle between the mirror and the laser beam. The inscription of the SRGs was monitored with a low-power (1 mW) 633 nm He–Ne laser and the diffraction efficiency of the first order diffracted beam was monitored.

For the confocal microscope the software zoom was kept fixed at seven, with a pixel size of 0.12 µm, 512 × 512 pixels per frame and pixel dwell time of 1.54 µs. The ROI size was of 4 × 200 pixels, oriented horizontally. A 488 nm wavelength laser was used to pattern, and a 633 nm laser was used to image the resulting morphology in widefield mode. The 20x air objective was used, leading to a maximum (100%) power density in the focal plane of 9.18 mW/cm^2 for the 488 nm laser.[46]

To image the SRGs, AFM was used to scan a 60 µm x 30 µm area with 128 horizontal lines, 512 points per line and scan speed of 0.12 Hz. When displaying 3D AFM images, the Z axis aspect ratio (defined as height divided by width) was set to 0.3, to better visualize the light inscribed patterns.

To obtain the pDR1m/PEDOT:PSS cross section FIB-SEM (Helios NanoLab 600i, Thermo Fischer, and LEO 1550, Zeiss) imaging was employed. The sample was sputtered with iridium for 60 s at 15 mA current and milled with gallium ion beam (tension: 30 kV for milling and 30 kV for polishing). Scanning electron micrographs were acquired in secondary electron mode with the electron beam to 3 kV.

Small Unilamellar Vesicles (SUVs) Preparation: The desired amount of 1-palmitoyl-2-oleoyl-sn-glycero-3-phosphocholine (POPC) lipid (Avanti Polar Lipids) with 0.1% (mol/mol) Texas Red 1,2-dihexadecanoyl-sn-glycero-3-phosphoethanolamine triethylammonium salt (TR) (Thermo Fisher, USA) as fluorescent probe was dissolved in chloroform. The solvent was evaporated under a constant flow of nitrogen, forming a homogeneous lipid film. The remaining solvent residues were removed by placing the samples in a desiccator under vacuum for 1 h. The resulting lipid film was rehydrated with DPBS buffer (1x) (pH 7.4) to obtain a final concentration of 5 mg/mL. The solution was gently vortexed and then sonicated on ice for 30 min. Finally, the suspension was extruded 15 times through a polycarbonate membrane with 50 nm pores using a mini-extruder (Sigma-Aldrich, USA) to obtain a SUV solution, which was stored at 4 °C for further experiments.[39]

SLB Formation: Lipid bilayers on different substrates were formed by the vesicle fusion method.[40] Briefly, the 0.5 mg mL^{-1} SUV solution was added to the electrochemical cell and incubated for 20 min, then the buffer was exchanged with DI water and incubated for 40 min. After the formation of the lipid bilayer on the pDR1m/PEDOT:PSS surface, the rest of the liposomes were replaced by DPBS buffer (1x) (pH 7.4) for electrochemical and FRAP experiments.[22]

Supported Lipid Bilayer (SLB) Electrochemical Characterization: Cyclic voltammetry (CV) and electrochemical impedance spectroscopy (EIS) were measured on a BioLogic potentiostat (SP-300, BioLogic Systems, Grenoble, France). The pDR1m/PEDOT:PSS /SLB was used as the working electrode, and a Pt wire and saturated Ag/AgCl electrode were used as the auxiliary and reference electrodes, respectively. Cyclic voltammograms were recorded in the potential range from − 1 to + 1 V versus Ag/AgCl and 50 mV/s as a scan rate. The EIS was recorded in the range 10^{-1} to 10^6 Hz, using a sinusoidal input voltage with amplitude of 50 mV, with 0 V offset.

FRAP: The fluidity of the POPC lipid bilayer with 0.1 mol% TR was assessed with the FRAP technique using a LSM 880 confocal laser scanning microscope with Airyscan (Carl Zeiss Germany) with a 20× objective. A defined area was photobleached with a 15 mW 561 nm laser beam to

assess membrane fluidity, and the recovery of fluorescence intensity was measured.

Statistical Analysis: Unless stated otherwise, the data were not preprocessed and are represented as mean ± standard deviation. A Github link to the python code used for the analysis can be found in Supporting Information. For AFM investigations, in each sample a $5 \times 5\ \mu m^2$ area was imaged, and from it 5 smaller $1 \times 1\ \mu m^2$ areas were analyzed using the AFM software to measure Rq, Ra, Rmax, which are indicators of surface roughness. For thickness and Young's modulus characterization of the layers, three measurements for each of the three replicates were used, for a total sample size of nine for each case. The thickness was then calculated with the software of the instrument used, and Young's modulus was calculated using the DMT model.

To determine the thickness of PEDOT:PSS on top of the pDR1m layer through FIB-SEM, six measurements were taken through ImageJ from a cross section of the pDR1m/PEDOT:PSS bilayer.

The analysis of the contact angle was made through the software of the instrument, fitting the droplet shape with a circumference, and measuring the tangent angle intersection with the plane of the surface. In total three different contact angle measurements were carried out, one for each replicate with the same conditions.

The absorption spectra were acquired with a 1 nm wavelength step, filtered with a Savitzky–Golay filter (25 data points window, first order polynomial) in a Python code, to reduce the noise influence when measuring the spectra of thin polymer layers. One spectrum for each case was analyzed.

Three replicates were analyzed with CV and three replicates for EIS characterizations, however here only one exemplary data set was shown in Figure 1f,g–i,j. For EIS investigations, the data sets were fitted using custom Python code to determine the various parameters. For the bidirectional scanning patterns, the prominence and width of the reliefs were analyzed using a custom Python code. The code draws 11 cross sections perpendicularly to the ROIs orientation, and for each calculates the width and prominence.

For the monodirectional scanning ones, the prominence of the patterns was calculated with the AFM software, taking three measurements along parallel cross sections compared to the ROI orientation and three along perpendicular ones. In the same way, three measurements for parallel width and three for perpendicular width were calculated.

For each set of parameters, two replicates of SRGs were analyzed, giving a total sample size of 22 for each of the bidirectional scanning patterns, and 12 for the monodirectional ones.

The fluorescence intensity of the spots in Figure 4 was measured and normalized to a reference spot in each image. The normalized fluorescence intensity was adjusted using a Bessel function.[41] Images were analyzed using the ImageJ Radial profile tool, which allowed quantification of fluorescence intensity along the radius of a selected area. The diffusion coefficient was determined using the following equation: $D = \omega^2/4\tau_{1/2}$, where ω is the radius of the photobleached spot and $\tau_{1/2}$ is the time needed to reach half of the maximum recovery intensity.[39] The EIS curves were also here fitted with the custom Python code for the previous EIS.

Supporting Information

Supporting Information is available from the Wiley Online Library or from the author.

Acknowledgements

Francesca Santoro and Ziyu Gao acknowledge funding from the European Research Council (ERC) under the European Union's Horizon 2020 research and innovation programme (BRAIN-ACT, Grant agreement No. 949478). Lasse Hyldgaard Klausen acknowledges funding from the Carlsberg Foundation (CF19-0742). Arri Priimagi and Chiara Fedele acknowledge the financial support given by the Emil Aaltonen Foundation (ABioT project) and by the Academy of Finland (LIBER Center of Excellence, No. 346107 and the PREIN Flagship Programme, No. 320165).

Open access funding enabled and organized by Projekt DEAL.

Conflict of Interest

The authors declare no conflict of interest.

Author Contributions

L.T. and Z.G. contributed equally to this work. L.T. and Z.G. contributed equally to the experimental design, data collection, analysis, and manuscript writing. M.R. contributed to engineering SLBs and electrochemistry analysis. C.F. and A.P. supported on interference lithography. L.H.K. provided AFM support on mechanical characterization C.L.B. contributed to interface visualization with focused ion beam-scanning electron microscopy. F.S. contributed to project design, supervision, data discussion, manuscript revision and funding acquisition. All the authors contributed to the data discussion and manuscript revision.

Data Availability Statement

The data that support the findings of this study are available from the corresponding author upon reasonable request.

Keywords

deformable bioelectronics, light-driven polymers, PEDOT:PSS, pop-up structures, supported lipid bilayers (SLBs), surface relief grating

Received: November 1, 2023
Revised: May 31, 2024
Published online: August 9, 2024

[1] R. Wu, M. Matta, B. D. Paulsen, J. Rivnay, *Chem. Rev.* **2022**, *122*, 4493.
[2] R. B. Rashid, A. M. Evans, L. A. Hall, R. R. Dasari, E. K. Roesner, S. R. Marder, D. M. D'Allesandro, W. R. Dichtel, J. Rivnay, *Adv. Mater.* **2022**, *34*, 2110703.
[3] D. T. Simon, E. O. Gabrielsson, K. Tybrandt, M. Berggren, *Chem. Rev.* **2016**, *116*, 13009.
[4] I. B. Dimov, M. Moser, G. G. Malliaras, I. McCulloch, *Chem. Rev.* **2022**, *122*, 4356.
[5] R. Elnathan, M. G. Barbato, X. Guo, A. Mariano, Z. Wang, F. Santoro, P. Shi, N. H. Voelcker, X. Xie, J. L. Young, Y. Zhao, W. Zhao, C. Chiappini, *Nat. Rev. Mater.* **2022**, *7*, 953.
[6] Y. Zhou, Y. Zheng, T. Wei, Y. Qu, Y. Wang, W. Zhan, Y. Zhang, G. Pan, D. Li, Q. Yu, H. Chen, *ACS Appl. Mater. Interfaces* **2020**, *12*, 5447.
[7] P. Shokoohimehr, B. Cepkenovic, F. Milos, J. Bednár, H. Hassani, V. Maybeck, A. Offenhäusser, *Small* **2022**, *18*, 2200053.
[8] P. Li, S. Kim, B. Tian, *ACS Nano* **2022**, *16*, 19651.
[9] I. R. Minev, *J. Polym. Sci.* **2023**, *61*, 1707.
[10] B. Yang, Y. Ji, F. Cai, H. Yu, *ACS Appl. Mater. Interfaces* **2023**, *15*, 23804.
[11] W. Jo, H. S. Kang, J. Choi, J. Jung, J. Hyun, J. Kwon, I. Kim, H. Lee, H. T. Kim, *Nano Lett.* **2021**, *21*, 5500.
[12] I. K. Januariyasa, F. Borbone, M. Salvatore, S. L. Oscurato, *ACS Appl. Mater. Interfaces* **2023**, *15*, 43183.
[13] S. De Martino, W. Zhang, L. Klausen, H. Y. Lou, X. Li, F. S. Alfonso, S. Cavalli, P. A. Netti, F. Santoro, B. Cui, *Nano Lett.* **2020**, *20*, 577.
[14] S. Oscurato, M. Salvatore, P. Maddalena, A. Ambrosio, *Nanophotonics* **2018**, *7*, 1387.

[15] F. Milos, G. Tullii, F. Gobbo, F. Lodola, F. Galeotti, C. Verpelli, D. Mayer, V. Maybeck, A. Offenhäusser, M. R. Antognazza, *ACS Appl. Mater. Interfaces* **2021**, *13*, 23438.
[16] F. Corrado, U. Bruno, M. Prato, A. Carella, V. Criscuolo, A. Massaro, M. Pavone, A. B. Muñoz-García, S. Forti, C. Coletti, O. Bettucci, F. Santoro, *Nat. Commun.* **2023**, *14*, 6760.
[17] S. J. Singer, G. L. Nicolson, *Science* **1972**, *175*, 720.
[18] D. Casares, P. V. Escribá, C. A. Rosselló, *Int. J. Mol. Sci.* **2019**, *20*, 2167.
[19] E. A. Schafer, E. Davis, Z. Manzer, S. Daniel, J. Rivnay, *ACS Appl. Mater. Interfaces* **2023**, *15*, 24638.
[20] S. T. Keene, C. Lubrano, S. Kazemzadeh, A. Melianas, Y. Tuchman, G. Polino, P. Scognamiglio, L. Cinà, A. Salleo, Y. van de Burgt, F. Santoro, *Nat. Mater.* **2020**, *19*, 969.
[21] D. Lee, W. H. Jung, S. Lee, E.-S. Yu, T. Lee, J. H. Kim, H. S. Song, K. H. Lee, S. Lee, S.-K. Han, M. C. Choi, D. J. Ahn, Y.-S. Ryu, C. Kim, *Nat. Commun.* **2021**, *12*, 3741.
[22] Y. Zhang, S. Inal, C.-Y. Hsia, M. Ferro, M. Ferro, S. Daniel, R. M. Owens, *Adv. Funct. Mater.* **2016**, *26*, 7304.
[23] M. Kawan, T. C. Hidalgo, W. Du, A.-M. Pappa, R. M. Owens, I. McCulloch, S. Inal, *Mater. Horiz.* **2020**, *7*, 2348.
[24] P. Urban, S. D. Pritzl, D. B. Konrad, J. A. Frank, C. Pernpeintner, C. R. Roeske, D. Trauner, T. Lohmüller, *Langmuir* **2018**, *34*, 13368.
[25] M. Doroudgar, J. Morstein, J. Becker-Baldus, D. Trauner, C. Glaubitz, *J. Am. Chem. Soc.* **2021**, *143*, 9515.
[26] M. L. DiFrancesco, F. Lodola, E. Colombo, L. Maragliano, M. Bramini, G. M. Paternò, P. Baldelli, M. D. Serra, L. Lunelli, M. Marchioretto, G. Grasselli, S. Cimò, L. Colella, D. Fazzi, F. Ortica, V. Vurro, C. G. Eleftheriou, D. Shmal, J. F. Maya-Vetencourt, C. Bertarelli, G. Lanzani, F. Benfenati, *Nat. Nanotechnol.* **2020**, *15*, 296.
[27] V. Vurro, M. Moschetta, G. Bondelli, S. Sardar, A. Magni, V. Sesti, G. M. Paternò, C. Bertarelli, C. D'Andrea, G. Lanzani, *Membranes* **2023**, *13*, 538.
[28] M. Barkey, R. Büchner, A. Wester, S. D. Pritzl, M. Makarenko, Q. Wang, T. Weber, D. Trauner, S. A. Maier, A. Fratalocchi, et al., **n.d**.
[29] N. A. Shahrim, Z. Ahmad, A. W. Azman, Y. F. Buys, N. Sarifuddin, *Mater. Adv.* **2021**, *2*, 7118.
[30] L. A. A. Pettersson, S. Ghosh, O. Inganäs, *Org. Electron.* **2002**, *3*, 143.
[31] E. A. Campo, in *Selection of Polymeric Materials* (Ed: E. A. Campo), William Andrew Publishing, Norwich, NY **2008**, pp. 103–140.
[32] *Surface Texture: Surface Roughness, Waviness, and Lay*, American Society of Mechanical Engineers, New York **2020**.
[33] S. Zhang, P. Kumar, A. Nouas, F. Laurie, H. Tang, F. Cicoira, *APL Mater.* **2015**, *3*, 014911.
[34] M. J. Donahue, A. Sanchez-Sanchez, S. Inal, J. Qu, R. M. Owens, D. Mecerreyes, G. G. Malliaras, D. C. Martin, *Mater. Sci. Eng.: R: Rep.* **2020**, *140*, 100546.
[35] A. F. Wibowo, J. W. Han, J. H. Kim, A. Prameswati, S. A. N. Entifar, J. Park, J. Lee, S. Kim, D. C. Lim, Y. Eom, M.-W. Moon, M.-S. Kim, Y. H. Kim, *ACS Appl. Mater. Interfaces* **2023**, *15*, 18134.
[36] R. Sarabia-Riquelme, W. C. Schimpf, D. L. Kuhn, M. C. Weisenberger, *Synth. Met.* **2023**, *297*, 117399.
[37] P. Karageorgiev, D. Neher, B. Schulz, B. Stiller, U. Pietsch, M. Giersig, L. Brehmer, *Nat. Mater.* **2005**, *4*, 699.
[38] N. Hurduc, B. C. Donose, A. Macovei, C. Paius, C. Ibanescu, D. Scutaru, M. Hamel, N. Branza-Nichita, L. Rocha, *Soft Matter* **2014**, *10*, 4640.
[39] E. T. Castellana, P. S. Cremer, *Surf. Sci. Rep.* **2006**, *61*, 429.
[40] P. S. Cremer, S. G. Boxer, *J. Phys. Chem. B* **1999**, *103*, 2554.
[41] N.-J. Cho, C. W. Frank, B. Kasemo, F. Höök, *Nat. Protoc.* **2010**, *5*, 1096.
[42] L. Simonsson, A. Gunnarsson, P. Wallin, P. Jönsson, F. Höök, *J. Am. Chem. Soc.* **2011**, *133*, 14027.
[43] M. Ravandeh, H. Kahlert, H. Jablonowski, J.-W. Lackmann, J. Striesow, V. Agmo Hernández, K. Wende, *Sci. Rep.* **2020**, *10*, 18683.
[44] M. Ravandeh, D. Thal, H. Kahlert, K. Wende, M. Lalk, *J. Solid State Electrochem.* **2020**, *24*, 3003.
[45] V. Atanasov, N. Knorr, R. S. Duran, S. Ingebrandt, A. Offenhäusser, W. Knoll, I. Köper, *Biophys. J.* **2005**, *89*, 1780.
[46] D. Grünwald, S. M. Shenoy, S. Burke, R. H. Singer, *Nat. Protoc.* **2008**, *3*, 1809.